A One-Pot Solid-State Synthesis of MgO Nanoparticles and their Catalytic, Biological, and Electrochemical Sensor Activities: Hexaaquamagnesium(II) Bis(6-oxo-1,6-dihydropyridine-3-carboxylate) as a Tool

Journal:	*New Journal of Chemistry*
Manuscript ID	NJ-ART-11-2022-005382.R1
Article Type:	Paper
Date Submitted by the Author:	05-Jan-2023
Complete List of Authors:	Balakrishnan, Prabha Devi; PSGR Krishnammal College for Women, Chemistry Natarajan, Arunadevi; PSGR Krishnammal College for Women, Department of Chemistry Rath, Nigam; University of Missouri-St Louis, Chemistry and Biochemistry P, Kanchana; PSGR Krishnammal College for Women, CHEMISTRY Thathan, Premkumar; Sungkyunkwan University College of Natural Science, Department of Chemistry

ARTICLE

Received 00th January 20xx,
Accepted 00th January 20xx

DOI: 10.1039/x0xx00000x

A One-Pot Solid-State Synthesis of MgO Nanoparticles and their Catalytic, Biological, and Electrochemical Sensor Activities: Hexaaquamagnesium(II) Bis(6-oxo-1,6-dihydropyridine-3-carboxylate) as a Tool

Prabha Devi Balakrishnan,[a] Natarajan Arunadevi,[a] Nigam P. Rath,[b] Ponnusamy Kanchana,[a]*Thathan Premkumar,*[c]

A new divalent Mg complex, hexaaquamagnesium(II) bis(6-oxo-1,6-dihydropyridine-3-carboxylate) ($[Mg(H_2O)_6](C_6H_4NO_3)_2$) **(1)**, was synthesized by reacting $Mg(NO_3)_2.6H_2O$ with 6-hydroxypyridine-3-carboxylic acid (6-hpca) in the presence of aminoguanidine bicarbonate. Here, **1** was studied by elemental, infrared (IR), ^{1}H NMR, ^{13}C NMR, ultraviolet-visible (UV–vis), thermal, and single-crystal X-ray diffraction (SC-XRD) analyses. We discovered that **1** crystallized in the triclinic P-1 space group, whereas the Mg(II) ion exhibited six coordinated water molecules with octahedral geometry. Interestingly, **1** was used as a solid-state precursor for synthesizing Mg oxide (MgO) nanoparticles (NPs). Fourier transform infrared (FT-IR), UV–vis, powder-XRD, TEM, and energy-dispersive X-ray spectroscopic analyses were performed on the prepared MgO NPs. The results showed that the as-prepared MgO NPs were small (14 nm) and homogeneous. The antibacterial activity and antioxidant scavenging assays of 6-hpca, **1**, and the MgO NPs against 2,2-diphenyl-1-picrylhydrazyl (DPPH) revealed that the MgO NPs had good biological properties. Furthermore, a sensitive electrochemical sensor was developed for improved glucose detection by modifying the glassy carbon electrode with as-prepared MgO NPs. MgO NPs demonstrated effective catalytic properties for the reduction of 4-nitrophenol to 4-aminophenol. The proposed approach is simple, environmentally friendly, and user-friendly.

Introduction

Alkaline earth metal complexes have piqued the interest of many chemists due to their wide range of applications in biological science, material science, catalysis, adsorption, and luminescence.[1-10] Magnesium appears to be the earth's third most abundant structural metal. Magnesium, an alkaline earth metal, is essential in all living systems.[11] Because of the nucleophilic nature of magnesium, magnesium complexes are known for their reactivity and can enhance the catalytic activity of metal nonmaterial.[12] Because of the abundance of magnesium in the earth's crust and its use in catalysis, the synthesis of magnesium complexes and their catalytic studies have piqued the interest of many researchers.[13] Metal complexes, in general, speed up the action and efficacy of drugs. The activity of metal complexes is determined by the ligand and metal ion present.

Pyridine carboxylic acids are found in niacin (vitamin B_3), a water-soluble vitamin, which is present in plant and animal tissues. Hydroxy-nicotinic acid (hydroxypyridine-3-carboxylic acid), a derivative of pyridine carboxylic acid, is a versatile and

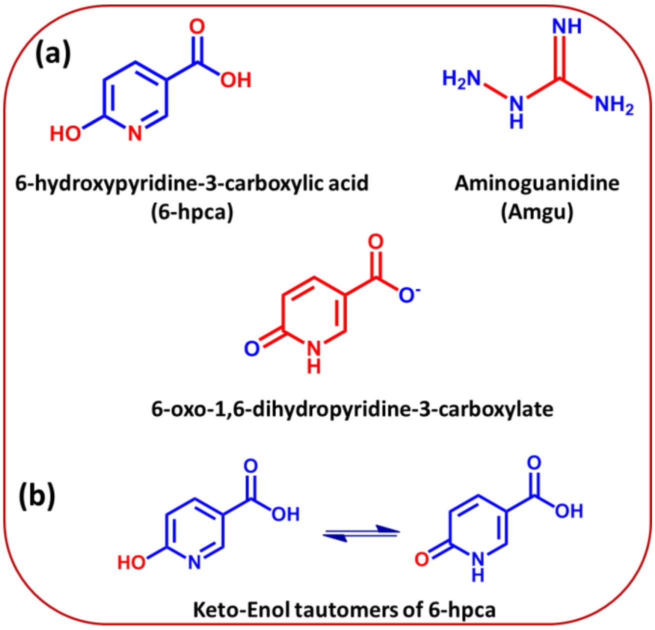

Fig. 1. Structures of (a) 6-hydroxypyridine-3-carboxylic acid (6-hpca); aminoguanidine; and 6-oxo-1,6-dihydropyridine-3-carboxylate anion. (b) Enol-keto tautomers of 6-hpca.

---

[a] *Department of Chemistry, PSGR Krishnammal College for Women, Coimbatore, Tamilnadu, India. E-mail: kanchana@psgrkcw.ac.in*
[b] *Department of Chemistry and Biochemistry and Center for Nanoscience, University of Missouri- St. Louis One University Boulevard, St. Louis, MO, USA*
[c] *The University College, Department of Chemistry, Sungkyunkwan University, Suwon, Gyeonggi 16419, South Korea. E-mail: thathanpremkumar@gmail.com*

Electronic Supplementary Information (ESI) available: Materials and methods, bond length and bond angle for complex 1, TG-DTA data, and EDX data. See DOI: 10.1039/x0xx00000x interesting ligand with multiple proton donor-acceptor sites. The anion has one pyridine ring with N and a carboxylate and phenolic group with three O atoms, which can exhibit various bonding geometrics.

Furthermore, nanotechnology has important and fascinating applications in catalysis, medicine, electronics, communications, engineering, environmental, and energy.[14,15] Magnesium compounds are used as precursors for nanomaterial synthesis[16-21], but most of the techniques used to prepare MgO nanoparticles (NPs) are costly and involve complex experimental procedures. Researchers are interested in MgO nanomaterials because of their diverse applications in catalysis, supercapacitors, refractory materials, and paints.[22-28]

This study aimed to characterize **1** using various physiochemical techniques after synthesizing it with 6-hydroxypyridine-3-carboxylic acid (6-hpca) in the presence of aminoguanidine (Amgu). Although the prepared complex was identified through analytical, spectral, and thermal studies, SC-XRD studies confirmed its structure. In addition, **1** was evaluated for biomedical applications such as antibacterial and antioxidant DPPH radical-scavenging activities. We also demonstrated that the as-prepared **1** could be used as a single-source solid-state precursor for MgO NP production. Impurities were not found in the metal oxides produced using this simple method. To prepare the MgO NPs, we used a relatively simple calcination method (thermal decomposition). The as-prepared MgO NPs demonstrated excellent catalytic activity, electrochemical sensing behavior toward glucose, and antibacterial and antioxidant scavenging properties.

Results and discussion

Metal salts react with heteroaromatic carboxylic acids at low pH to form metal complexes. Scheme 1 depicts the reaction of 6-hpca and the Mg salt in the presence of Amgu. Complexation was accomplished by reacting one part metal salt with one part 6-hpca and Amgu in a water bath at reflux for 6 h. Notably, Amgu played an important role in synthesizing **1** in a suitable crystalline form by keeping the pH of the solution (pH 5) stable to form crystals. Notably, the preparation of **1** in the absence of Amgu was unsuccessful. The Mg complex was separated as a colorless single-crystal that could be analyzed using SC-XRD. Water, alcohol, dimethyl formamide, and DMSO were all soluble in the synthesized compound. Complex **1** has the molecular formula $[Mg(H_2O)_6](C_6H_4NO_3)_2$, and elemental analysis and metal estimation confirmed its composition. Through a simple thermal decomposition process, the Mg complex was used as an efficient solid-state precursor for forming MgO NPs. This is the first report to our knowledge on the synthesis of **1** and its use as a solid source precursor for the formation of MgO NPs.

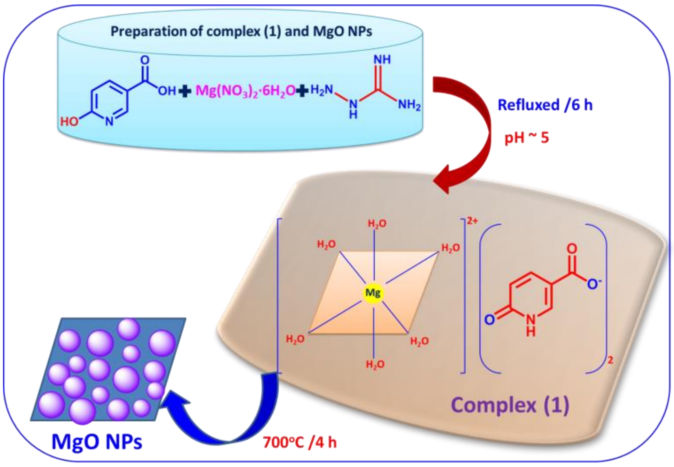

Scheme 1. Schematic representation of the preparation of **1** and the MgO NPs.

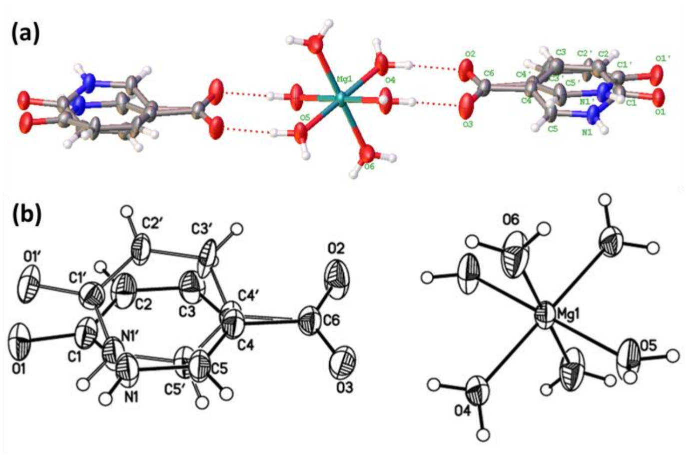

Fig. 2. (a) Molecular structure of **1**. (b) The Oak Ridge Thermal Ellipsoid Plot view of the molecule with 50% probability ellipsoids.

SC-XRD analysis of 1

SC-XRD was used to determine 1's molecular structure. According to this research, **1** crystallized in the triclinic crystal system of space group P-1 with Z = 1. Table 1 contains the crystal data, and Table S1 contains the important bond parameters. The movement of the hydrogen atom of the OH group to the nitrogen atom causes 6-hpca to exhibit keto-enol tautomerism (Fig. 1) in solid and solution states.[29-34] As a result, the independent unit contains a half hexaaquamagnesium(II) complex cation with the Mg(II) ion and one deprotonated keto form of the 6-hpca moiety, the 6-oxo-1,6-dihydropyridine-3-carboxylate anion (Fig. 1, a tautomer of the 6-hydroxypyridine-3-carboxylate anion). Overall, the crystal structure of **1** comprised an Mg(II) ion coordinated by six oxygen atoms from six water molecules and was free of acid units. Notably, the anions 6-oxo-1,6-dihydropyridine-3-carboxylate were not coordinated to the Mg ion but instead functioned as charge-compensating anions (two units of acid moieties, each acting as a carboxylate anion). The six oxygen atoms (O4, O5, O6, O4′, O5′, and O6′) of the H_2O molecule occupy the basal and apical coordination positions. O4 lies on the mirror plane bisecting the O5-Mg(II)-O5′. The octahedral geometry surrounding the Mg atom was slightly distorted. Figures 2a and b show the molecular structure with atomic labeling and the projection view of the molecule with 50% probability ellipsoids of **1**.

Table 1. Crystal data and structure refinement for **1**.

Identification code	Mg complex
Empirical formula	$C_{12}H_{20}MgN_2O_{12}$
Formula weight	408.61
Temperature	300(2) K
Wavelength	0.71073 Å
Crystal system	Triclinic
Space group	P-1
Unit cell dimensions	a = 7.5814(2) Å α= 88.9529(16)°.
	b = 7.6005(3) Å β= 80.0769(13)°.
	c = 7.6221(3) Å γ = 88.2066(14)°.
Volume	432.38(3) $Å^3$
Z	1
Density (calculated)	1.569 Mg/m^3
Absorption coefficient	0.172 mm^{-1}
F(000)	214
Crystal size	0.188 x 0.136 x 0.099 mm^3
Theta range for data collection	2.681 to 26.368°.
Index ranges	$-9 \le h \le 9$, $-9 \le k \le 9$, $-9 \le l \le 9$
Reflections collected	4730
Independent reflections	1761 [R(int) = 0.024]
Completeness to theta = 25.242°	99.2 %
Absorption correction	Semi-empirical from equivalents
Max. and min. transmission	0.8620 and 0.7974
Refinement method	Full-matrix least-squares on F^2
Data/restraints/parameters	1761/109/185
Goodness-of-fit on F^2	1.159
Final R indices [I>2 sigma(I)]	R1 = 0.0393, wR2 = 0.0986
R indices (all data)	R1 = 0.0438, wR2 = 0.1014
Largest diff. peak and hole	0.182 and −0.228 e.$Å^{-3}$

A complex $[Mg(H_2O)_6]^{2+}$ cation with a discrete 6-oxo-1,6-dihydropyridine-3-carboxylate anion is present in the crystal structure (Fig. 2). This suggests that the 6-hydroxypyridine-3-carboxylate anion was present in its pyridone form (keto form), that is, as the isomer with a keto group and a protonated N atom. The presence of the Mg ion and the water molecule's hydroxyl group resulted in the formation of N-H---O and O-H---O hydrogen bonds[35-39] (Fig. 3). Several N-H---O and O-H---O hydrogen-bond formations were used to achieve the crystal packing. The N1-H1---O hydrogen bonds formed a one-dimensional (1D) chain structure between the carboxylate anions. The two adjacent chains were further linked using H2O molecules via O4-H4---O3 and O5-H5---O2 interactions, resulting in an extended chain. The packing pattern demonstrated strong interlocking of the cationic and anionic moieties via a multidirectional hydrogen-bonding network, resulting in a three-dimensional (3D) structure (Fig. 3).

Infrared spectrum

The FT-IR spectrum of **1** (Fig. 4a) exhibited an intense broad peak at 3544 cm^{-1} assigned to the O–H stretching band of coordinated water molecules. It also exhibited a band at 3168 cm^{-1}, revealing the existence of the N–H group. The symmetric and asymmetric stretching frequencies of the carboxylate group appeared in the regions 1340 and 1578 cm^{-1}, respectively. The peak at 1229 cm^{-1} was attributed to the C–N of the pyridine ring.

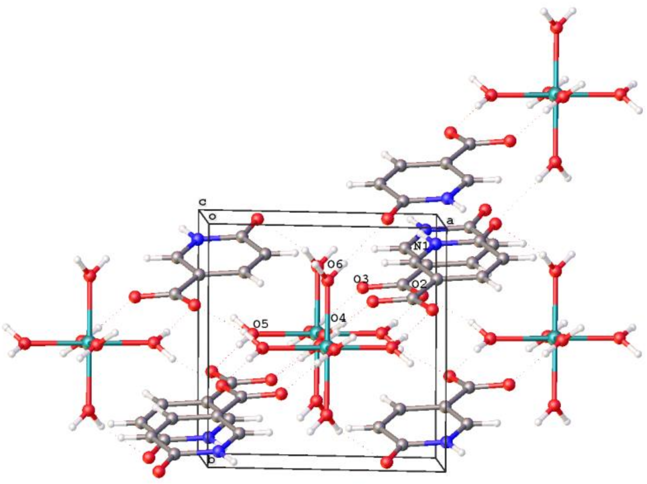

Fig. 3. Hydrogen-bonding networks and packing diagram between the hydrated Mg(II) cation and 6-hpca anion.

The ^{1}H and ^{13}C NMR spectra of 1

Figure 4b depicts the ^{1}H NMR spectrum of **1** in DMSO and TMS as an internal standard. The N–H proton was assigned the singlet at 13.48 δ. Multiplets in the 8.40–8.42 δ range were assigned to the C–H protons of the pyridine ring close to the carboxylate anion, while those in the 7.97–7.99 δ and 6.69–6.73 δ ranges were assigned to the C–H proton of the pyridine ring close to the N atom. In 1, the signal in the range of 2.52–2.54 δ was assigned to the O–H of the water molecules. These findings supported the successful synthesis of **1** and were consistent with the solid-state structure.

DMSO was used as the solvent for recording the ^{13}C NMR spectrum of **1**. Peaks in the ^{13}C NMR signals are seen in the expected regions. Peaks in the 115–159 ppm range are assigned to the aromatic ring's carbon atoms. The ^{13}C NMR peak for the -CO carbon near to NH group in **1** is obtained at 168 ppm. The carboxylate carbon atom is responsible for the peak in the 172-ppm range. The SC-XRD results corroborated these features.

Electronic spectra

Figures 5a and b show the UV–VIS spectrum and energy band gap (Tauc's plot) of **1**. They provided information on the transition range and band gap of **1**. Complex **1** had an absorption maximum at 238 nm, revealing the π → π* transition. In addition, **1** had a peak at 352 nm that was attributed to the ligand-to-metal charge transfer transition. E = 3.73 eV was calculated as the band gap energy.

Emission spectra

At room temperature, the photoluminescence property of free acid and **1** was investigated, as shown in Fig. 6a. A strong, broad emission band at 388 nm was observed, as well as an excitation band at 330 nm. The free 6-hpca showed luminescence with maximum emission at 380 nm, which corresponded to the n → π* transition. The deprotonation of the carboxylic acid moiety was attributed to the enhancement of the photoluminescence spectrum of complex **1** compared to

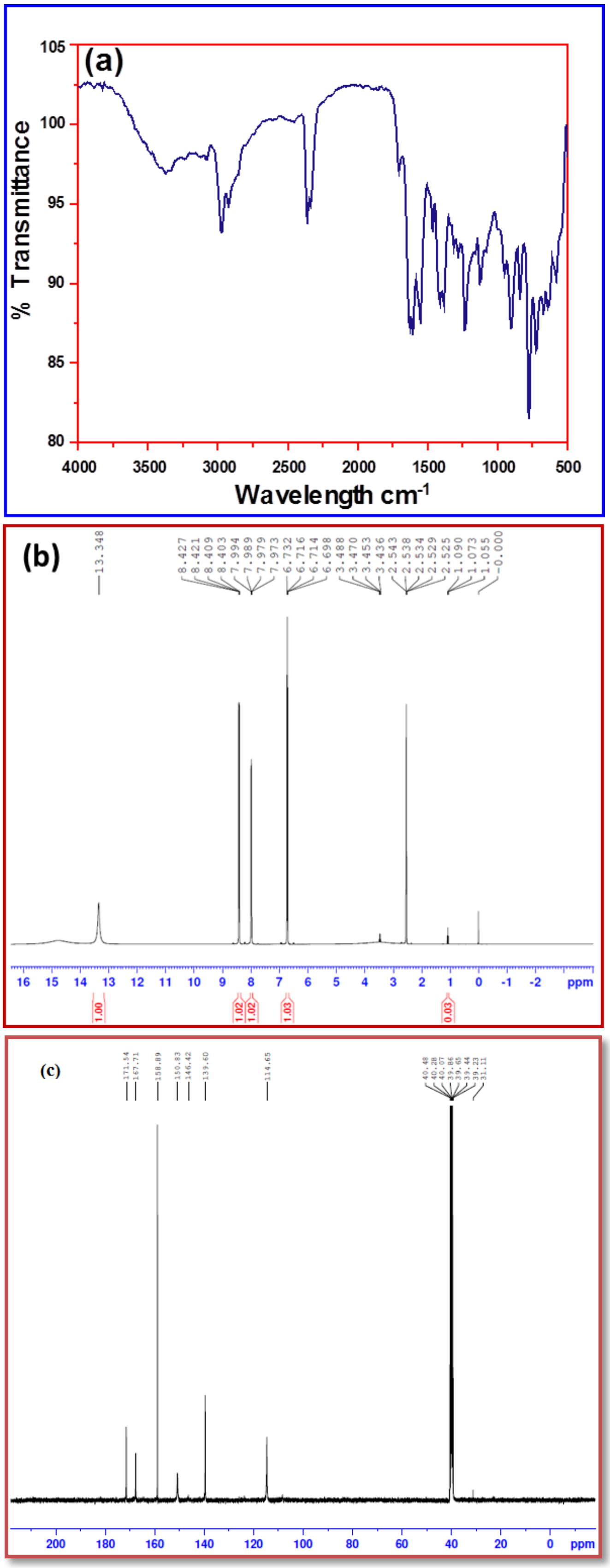

Fig. 4. (a) FT-IR, (b) ^{1}H NMR and (c) ^{13}C NMR spectra of complex **1**.

free 6-hpca. Complex **1** showed an increased redshift compared to the 6-hpca emission band, indicating that it is a potential luminescent material.

Thermal analysis

To determine the thermal reactivity of **1**, simultaneous TG-DTA was performed at temperatures ranging from 20°C to 900°C. Table S2 shows the results of the thermogram's continuous decomposition (Fig. 6b). The thermogram showed a 33% mass loss, corresponding to the loss of an oxopyridinium carboxylate moiety to produce an $Mg(H_2O)_6(C_6H_3NO_3)$ intermediate, which was reflected in the DTA spectra as an endothermic peak at 167°C. Furthermore, the $Mg(H_2O)_6(C_6H_3NO_3)$ intermediate decomposed continuously and endothermically to form MgO as the end residue.

Preparation of MgO NPs

The MgO NPs were fabricated by heating 5 g of **1** at 700°C in a muffle furnace with a silica crucible and calcined for 4 h. The main advantage of the current method of synthesizing MgO NPs using complex **1** is that it is a simple, single-source, one-pot, solid-state precursor method for synthesizing MgO NPs. Among other advantages, synthesizing MgO NPs by the thermal decomposition method is cleaner, easier, cheaper, and faster. Furthermore, all other organic moieties decompose during thermal decomposition, resulting in the formation of pure and nearly homogeneous MgO NPs. Because complex precursors eliminate the work of solvent removal, the purity of metal oxides is very high. The added benefit is that no by-products are formed, resulting in a higher yield and a smaller size. Furthermore, this method has its advantage due to its ability to prepare MgO NPs on a large scale and store them easily for a longer period. Because the MgO NPs were prepared in the solid-state, this technique is user-friendly, and no additional manipulative skills or methods are required to isolate the NPs in the solid-state, as opposed to tedious solution-based approaches. As a result, producing MgO nanostructures by thermal decomposition of metal complex precursors is one of the most convenient techniques because the resulting product allows us to avoid complicated synthesis procedures and conditions, as well as special instruments.

FT-IR, UV–VIS-Diffuse reflectance spectroscopy (DRS), and PXRD for the MgO NPs

The FT-IR spectrum of MgO NPs (Fig. 7a) revealed two major vibrational bands above 1000 cm^{-1}. The crystal vibrations of the Mg-O bond were responsible for two peaks at 3238 and 1579 cm^{-1}. A vibrational band around 702 cm^{-1} was observed, confirming the production of the MgO NPs.[40,41] The optical absorption properties of the MgO NPs were investigated by UV–VIS-DRS, and the corresponding absorption peaks are shown in Fig. 7b. The peak at 341 nm indicated the absorbance of MgO.[42-45]

CuKα radiation was used for PXRD in the 2θ range of 20–80°. Figure 7c depicts the XRD pattern of MgO NPs. Peaks at 36.88°, 42.75°, 62.23°, 74.54°, and 78.61°, which corresponded to the planes (111), (002), (202), (113), and (222), respectively, confirmed the formation of MgO's polycrystalline cubic phase (JCPDS card No. 87-0653). This was consistent with previous findings.[46-48] The XRD pattern revealed no additional peaks, confirming its purity. The highly crystalline nature of the synthesized nano MgO was attributed to the intense peak on the (002) plane. The average crystallite size was calculated using the Debye-Scherrer equation: $D = K\lambda/\beta Cos\theta$, where D is the average particle size of NPs, K is a Scherrer constant (0.9), λ is the X-ray wavelength (0.15406 nm), β is the full width at half maximum of the diffraction peak [most intense peak corresponding to the (002) plane] and θ is the incidence angle (peak position). The average crystallite size of the as-prepared MgO NPs was determined to be 17 nm by substituting the corresponding values into the Debye-Scherrer equation.

TEM

Figure 8a depicts TEM micrographs of MgO NPs. High-resolution TEM (HRTEM) was used to examine the surface morphologies and particle sizes of the as-prepared MgO NPs (Figs. 8b and c). The HRTEM images revealed that the MgO NPs were irregularly shaped, with an average particle diameter size of 14 nm (Fig. 8d), which is nearly consistent with the PXRD crystal size. Furthermore, the electron diffraction pattern of a selected area (SAED) in the TEM image revealed a remarkable ring-like pattern, indicating that the as-prepared MgO NPs are polycrystalline. The SAED pattern (Fig. 8c inset) obtained from the MgO NPs TEM image revealed five discernible diffraction rings corresponding to hkl values (111), (002), (202), (113), and (222), indicating the formation of the polycrystalline cubic phase of MgO, which is consistent with the PXRD pattern results (Fig. 7c). Furthermore, the energy-dispersive X-ray (EDX) spectrum of the MgO NPs (Fig. 8e) shows only Mg and O (Table S3), which is consistent with the PXRD (Fig. 9c) results.

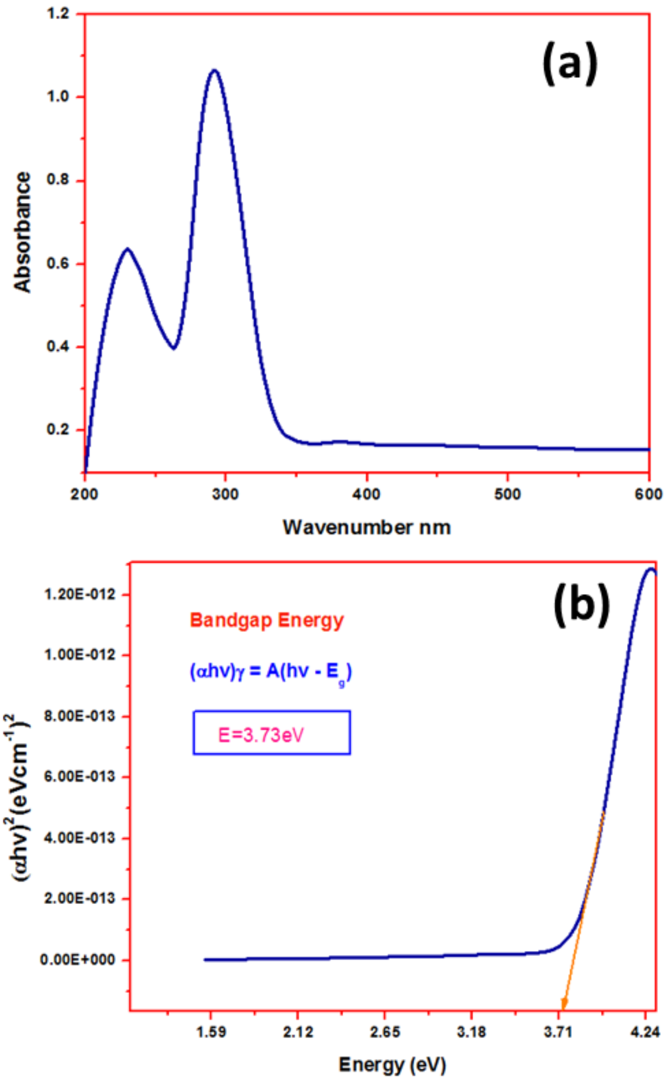

Fig. 5. (a) UV–VIS spectrum and (b) energy band gap (Tauc's plot) of complex **1**.

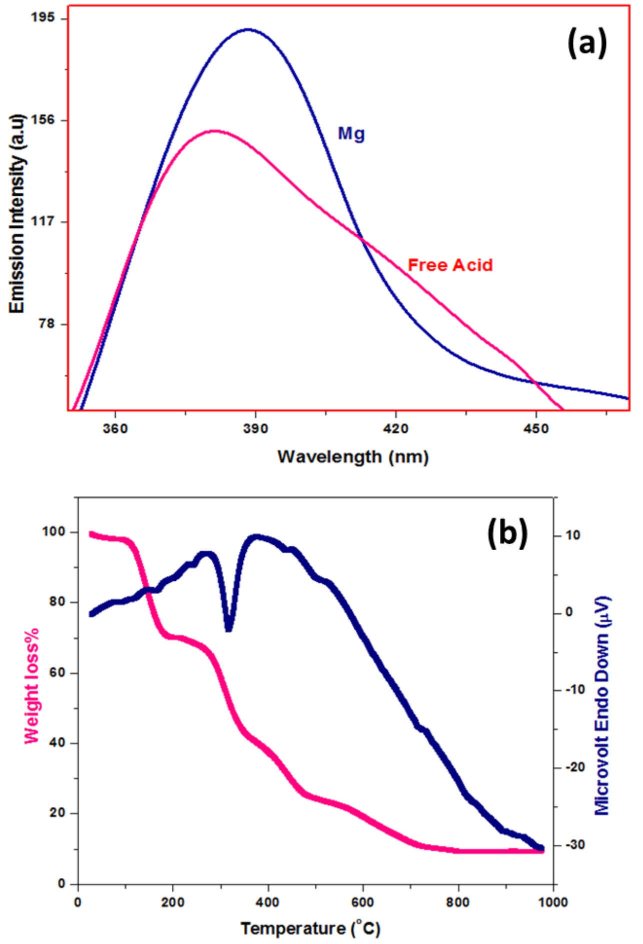

Fig. 6. (a) Emission spectra of 6-hpca and complex **1**. (b) Simultaneous TG-DTA curve of complex **1**.

Applications of 1 and the MgO NPs

Antibacterial studies

For *in vitro* biological screening, the well diffusion method was used. Using Kanamycin as a standard, the 6-hpca, **1**, and MgO NPs were tested against two pathogenic bacteria[49] (*Escherichia coli* (Gram-negative) and *Staphylococcus aureus* (Gram-positive)). Table 2 shows the inhibition zone (mm) for 6-hpca and the as-prepared compounds (**1** and MgO NPs) against bacterial growth. They were biologically active against the

Table 2. Antibacterial activity data of the 6-hpca, Mg complex (**1**) and MgO NPs.

Sample	Diameter of inhibition zone (mm)	
	Staphylococcus aureus	*Escherichia coli*
Kanamycin (standard drug)	25	30
6-hpca	14	18
Mg complex (**1**)	17	20
MgO NPs	22	25

bacterial species. However, 6-hpca demonstrated less activity when compared to **1** and MgO NPs. The higher zone of the inhibition of **1** than free acid is determined by the effect of metal ions on the cell process of microorganisms. The complex formation increases the metal ion's lipophilic property, which aids in the permeation of lipid layers in microorganism cells.[50] Complexes also affect respiration and inhibits protein synthesis, preventing further cell multiplication.[51,52] It has also been demonstrated that metal oxides have greater antimicrobial potency than their metal complexes. This is easily demonstrated because smaller particles typically have a higher surface-to-volume ratio, providing a more efficient means of antibacterial activity.[50]

Because of their smaller particles with a higher surface-to-volume ratio, MgO NPs inhibited antibacterial activities more effectively than free acid and **1**.[53] Although MgO NPs had higher antibacterial activity than **1**, they had slightly less activity than *Kanamycin* (the standard drug, positive control). MgO NPs, unlike most metal oxides, have distinct antibacterial properties due to their unique oxide vacancies and crystalline structure.[54-57] Tang et al. also demonstrated, using an antibacterial mechanism, that MgO NPs can be used as an antibacterial agent.[58] Many studies have shown that the antibacterial activity of MgO NPs is size-dependent.[59] As a result, the MgO NPs prepared in this study have the potential to be highly beneficial in antibacterial applications while posing less risk to the environment and humans.

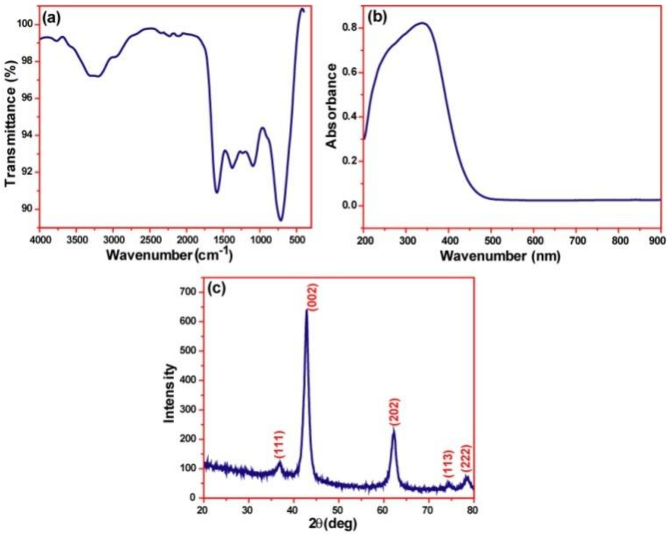

Fig. 7. (a) FT-IR, (b) UV–VIS-DRS spectra, and (c) PXRD pattern of the MgO NPs.

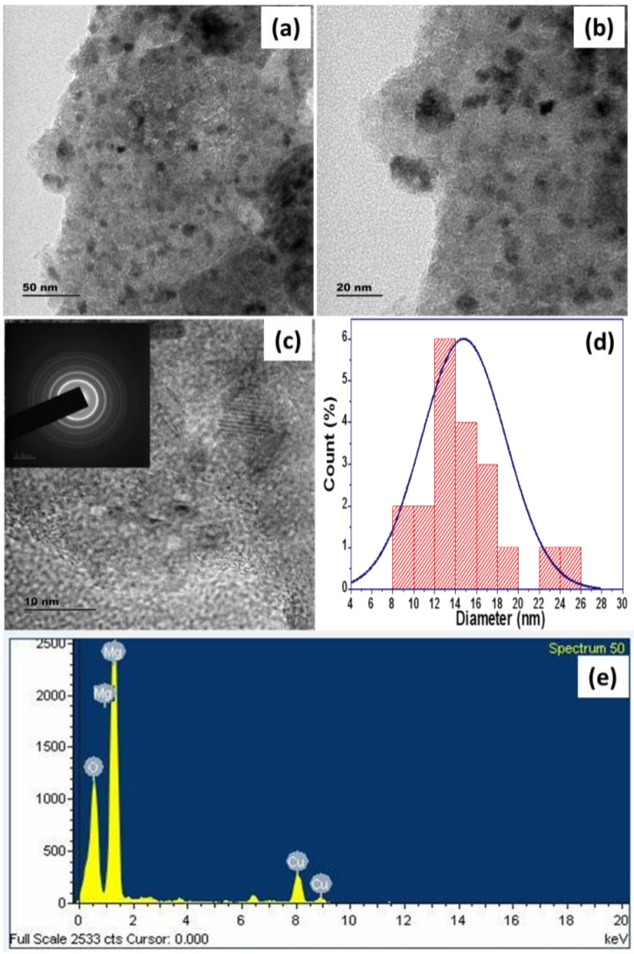

Fig. 8. (a) TEM and (b and c) HRTEM images of MgO NPs. (d) Size-distribution analysis and (e) EDX spectrum of the MgO NPs. The inset shows the SAED pattern of the MgO NPs.

Antioxidant studies

The DPPH radical absorbs strongly at 517 nm.[57] When solution **1** and the MgO NP solutions were mixed and incubated with DPPH, the DPPH solution changed color from dark violet to light yellow. This represented the reduction and conversion of stable DPPH into 1,1-diphenyl-2-picrylhydrazine via electron donation from metal compounds, resulting in a decrease in absorbance at 517 nm. The percentage of radical-scavenging ability increased with **1** concentration and its oxide NPs. Finally, the ascorbic acid standard's IC_{50} values were compared to those of **1** and the MgO NPs. MgO NPs had a high scavenging efficiency (Fig. 9), whereas **1** had a lower activity than MgO NPs. The higher scavenging behaviors of MgO NPs compared to **1** were attributed to their larger surface-to-volume ratio, resulting in better scavenging activity. In fact, the antioxidant activity of **1** is determined by its structure, specifically its ability to donate hydrogen. Complex **1** is compared to the complex of quercetin.[60,61] The antioxidant activity of **1** is determined by its molecular structure; however, complexation with metal ions may affect the chemical properties of ligand molecules, resulting in a variation in activity.[62] El-Sayyad et al. reported that MgO NPs have the highest inhibition value of 90% for DPPH radical-scavenging

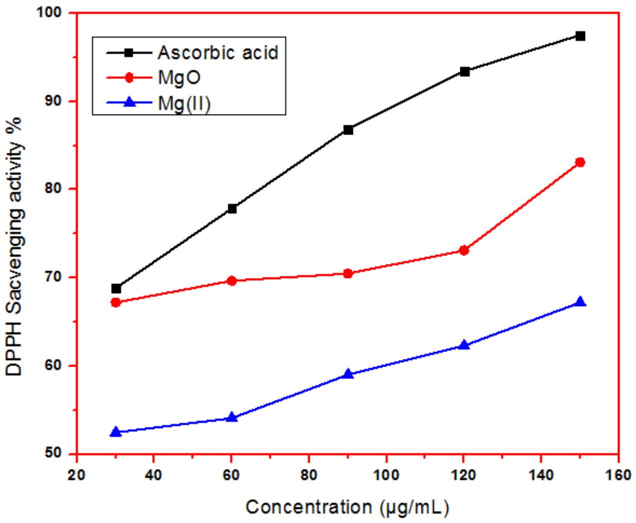

Fig. 9. Antioxidant activity of ascorbic acid, 1, and the MgO NPs on DPPH radicals.

activity.[63] Hosseini et al. also reported that adding MgO NPs had a significant effect on the antioxidant properties of the film, with the composite film containing the most MgO NPs having the highest antioxidant properties.[64] As a result, the findings obtained in this study are comparable and consistent with the previously reported works.

Electrochemical performance of the synthesized compounds

The electrochemical performance of **1** and the MgO NPs were evaluated with the glassy carbon electrode (GCE) electrodes in NaOH (0.1 M) at 100 mVs^{-1}. All the experiments were conducted at room temperature (Scheme 2). Effective redox responses and lower background currents were observed in the voltammograms of complex **1**, compared with those of its oxide in 0.1 M NaOH. Fig. 10a depicts the voltammograms.

Complex **1** contained an electroactive metal encapsulated in electroinert organic compounds, which reduced electron transfer and background current. Under alkaline conditions, MgO exhibited a remarkable redox property within 0.36–0.54 V vs. Ag/AgCl, indicating an increased electrochemical otential for the active metal oxide. Scheme 3 depicts the schematic diagram of the electrochemical setup detailed understanding of the study.

Electrocatalytic nonenzymatic glucose sensing

CV was used to investigate the nonenzymatic electrocatalytic biosensing activities of **1**, and the MgO NPs-modified with GCE in the presence and absence of different glucose concentrations (1, 2, 3, 4, and 5 mM) in a NaOH (0.1 M) solution at a scanning rate of 100 mVs^{-1} (Fig. 10).

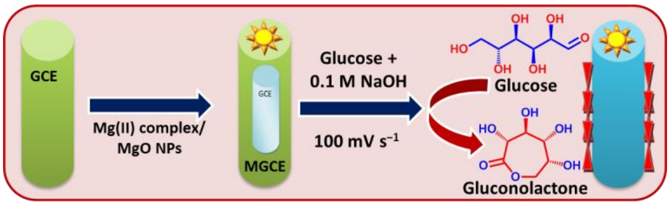

Scheme 2. Mg complex- or MgO NP-modified glassy carbon electrode as the working electrode.

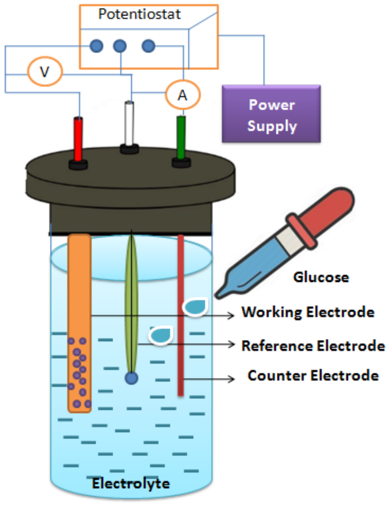

Scheme 3. Schematic diagram of the electrochemical setup.

There was no discernible redox process for **1** in the presence or absence of glucose (Figs. 10a and b), indicating that **1** exhibits no electrocatalytic activity for glucose sensing (Fig. 10b). Because of the oxidation of glucose into gluconolactone, the glucose electrooxidation wave of the MgO NP-modified GCE electrode appeared at 0.45 V with a well-resolved anodic peak (Fig. 10c). As a result, the MgO NPs had a higher anodic wave than the **1**, attributed to the excellent electron delivery system of Mg metal in its oxide. The MgO NPs exhibited slightly enhanced electrical conductivity (Fig. 10c) because of their nano architecture. The synergistic property of MgO NPs and hierarchical void spaces added significant space to the glucose analyte's adaptation. The increased activity of MgO NPs was due to their small size and homogeneity, which provided active metallic sites. For the determination of glucose, the MgO NPs electroactive species has a good detection limit of 0.45 V.

These findings suggested that MgO NPs-modified GCE could be used as a selective and sensitive glucose detection material. When the electroanalytical performance of the MgO NPs-based glucose sensor is compared to previous studies, the sensitivity is 0.56 V for MgO[65], 0.56 V for CuO, and 0.70 V for NiO carbon nanocomposites.[66-70] Furthermore, the composition of these materials can be altered with dopants to improve sensing behavior.

Catalytic reduction of 4-nitrophenol (4-NP)

The reduction reaction of 4-NP was performed with and without MgO NPs as the catalyst to evaluate their catalytic property. Because of the kinetic barrier between the 4-nitrophenolate anion and BH_4^- and the large potential variation between the electron donor and acceptor molecules, the reduction reaction remained unchanged in the absence of MgO NPs. The ability of 4-NP to be reduced to 4-aminophenol (4-AP) by $NaBH_4$ (sodium borohydride) in the presence of MgO NPs (catalyst) was monitored by recording changes in the

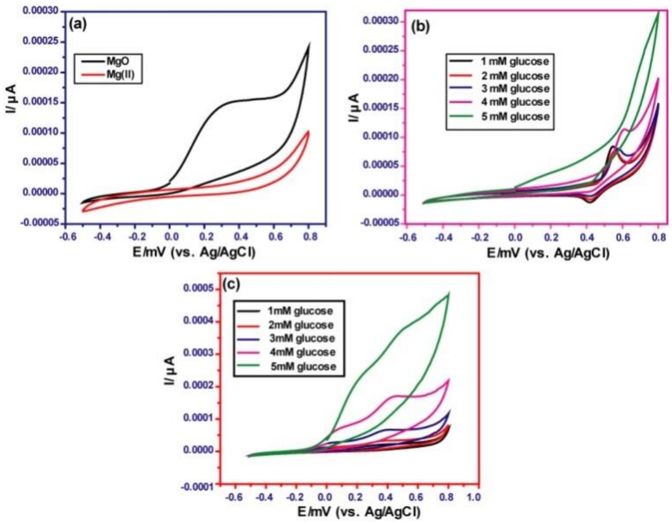

Fig. 10. (a) Cyclic voltammetry of the modified Mg complex (1) and MgO NPs in a NaOH (0.1 M) solution at a scan rate of 100 mV s−1. (b) Glucose electrooxidation of the Mg complex (1) at different glucose concentrations. (c) Glucose electrooxidation of the MgO NPs at different glucose concentrations in NaOH (0.1 M) at a scan rate of 100 mV s−1.

absorbance intensity bands. After adding NaBH4, the aqueous 4-NP solution changed from light to dark yellow. The bathochromic shift of the absorption peak from 318 to 400 nm (Fig. 11a) was ascribed to the formation of the phenolate ion under alkaline conditions[71] immediately after the addition of $NaBH_4$ to the solution. The main mechanisms responsible for the reduction process are proton accessibility and electron transferability. 4-AP is a well-known intermediate in various applications, including corrosion inhibitors, antipyretic drugs, anticorrosive lubricants, and photographic developers. The phenolate ion has superior π–conjugated donor-acceptor properties. The reduction is expected to be complete when the yellow solution becomes colorless. The intensity of the characteristic absorption peak at 400 nm decreased, with the formation of new absorption peaks at 309 nm, demonstrating the production of 4-AP (Fig. 11b). At this point, the yellow color of 4-NP had been completely bleached away, and the solution turned colorless, confirming the complete reduction of 4-NP to 4-AP. The particle size of the MgO NPs is critical in the reduction reaction. The reaction took about 48 min to complete.

Using pseudo-first-order kinetics, the rate constant of 4-NP reduction was calculated. $\mathbf{\ln(C_t/C_o) = \ln(A_t/A_o) = -kt}$, where k is the rate constant, C_t is the concentration ratio with time (t), C_o is the initial concentration at t = 0, A_o is the initial concentration of 4-NP, and A_t is the concentration of 4-NP at time t. The tangent slope of the linear plot was used to calculate the value of k at room temperature (Fig. 11c). In the presence of MgO NPs, k for 4-NP reduction was 0.05815 min^{-1}. After the reaction, the catalyst was recovered and reused five more times, increasing the reaction time due to the recycling of the catalyst (Fig. 11d). The conversion was calculated using the equation below and is shown in Table 3.

Table 3. Reaction completion time and percentage conversion of the MgO NPs.

Cycles	Reaction completion time (min)	%Conversion
1	48	96.9
2	52	95.9
3	60	95.4
4	68	89.4
5	76	87.6

$$\%\text{Conversion} = (A_o - A_t/A_o) \times 100$$

where A_o denotes the initial concentration of 4-NP and A_t denotes the concentration of 4-NP at time t.

The results demonstrated the potential for synthesizing an effective MgO NP catalyst in reduction reactions by modifying its chemical composition and particle size in the future. However, to our knowledge, no reports on 4-NP reductions with pure MgO NPs have been published. When compared to other metal oxides' 4-NP reduction, MgO NPs show good reduction toward 4-NP.[72-75]

Conclusions

A new Mg complex (**1**) was synthesized in a simple one-pot method at room temperature and structurally characterized using SC-XRD. To form a stable compound, the Mg(II) ion was coordinated with six water molecules to form the hexaaquamagnesium(II) complex ion, whose charge was compensated by bis(6-oxo-1,6-dihydropyridine-3-carboxylate) anions. The thermal decomposition of **1** continued indefinitely, yielding MgO NPs as the final residue. FT-IR, UV–vis-DRS, PXRD, HRTEM, and EDX studies confirmed the formation of pure single-phase cubic nano MgO. The antibacterial activity of 6-hpca, **1**, and MgO NPs against Gram-negative and positive bacterial pathogens was determined, and the final results

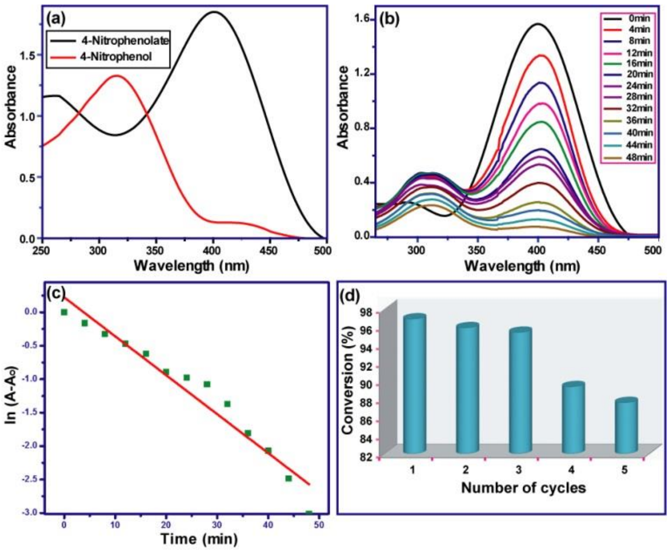

Fig. 11. (a) UV–VIS spectra of 4-NP in the absence and presence of $NaBH_4$. (b) Time-dependent UV–VIS spectral changes during the reduction of 4-NP catalyzed by the MgO NPs. (c) Plots of reaction time vs. $\ln(A_t/A_0)$. (d) The reusability (conversion efficiency of 4-NP in five successive cycles) of the MgO NPs as catalysts for the reduction of 4-NP to 4-AP.

showed that MgO NPs had a significant effect on the pathogens when compared to **1**. Furthermore, when compared to Staphylococcus aureus, MgO NPs had a greater zone of inhibition (25 mm) against E. *coli*. The antioxidant DPPH radical-scavenging property of **1** and MgO NPs was compared to that of ascorbic acid (standard). The data showed that the MgO NPs had good radical-scavenging activity, comparable to the standard result. Furthermore, MgO NPs demonstrated significantly higher electrocatalytic activity than **1** for glucose electrochemical reduction, indicating their potential as promising sensor materials. Furthermore, the MgO NPs were effective catalysts for potential applications, such as reducing 4-NP to 4-AP at room temperature. It was also confirmed that the MgO NP catalyst could be easily recovered from the reaction and reused for another five cycles with a conversion efficiency exceeding 80%. MgO NPs are typical basic oxides, with the lowest solubility among other alkaline earth metal oxides. As a result, we believe that MgO NPs are suitable candidates for reusable catalysts with no leaching. As a result, the aforementioned characteristics or properties of MgO NPs indicate their potential applications in various fields, such as small and bulk chemical preparations. However, it is currently only used in a few catalytic reactions. Furthermore, given the ease of preparation of the Mg complex and MgO NPs, as well as their catalytic, biological, and electrochemical sensor potential, this system is a promising platform for industrial and biomedical applications.

Experimental

Preparation of 1. Solid 6-hpca (0.139 g, 1 mmol) and Amgu bicarbonate (0.136 g, 1 mmol) were mixed in 20 mL of hot, double-distilled water and mechanically stirred until effervescence ceased. The pH of the resulting solution was 4. After that, $Mg(NO_3)_2.6H_2O$ (0.256 g, 1 mmol) was added to the clear solution and homogeneously stirred. The clear solution (pH ~ 5) was refluxed for 6 h and concentrated over a water bath to reduce it by one-fourth of its initial volume. After 1 week, transparent colorless rectangular crystals were isolated from the final solution and maintained at ambient temperature. After thoroughly washing the crystals with cold distilled ethanol, the crystals were dried under a vacuum. The crystals suitable for structural analysis were selected, and SC-XRD data were recorded. Amgu functioned as a pH-maintaining agent and an efficient catalyst to synthesize the desired product. The synthesis scheme is shown in Fig. 1. Elemental analysis (Calcd., %): C, 35.27; H, 4.93; N, 6.86; Mg, 5.59. $C_{12}H_{20}MgN_2O_{12}$ (Found, %): C, 35.24; H, 4.98; N, 6.82; Mg, 5.89 (by metal estimation). The melting point was 230°C.

Preparation of MgO NPs. After reaching a constant temperature and calcining for 4 h, the magnesium complex (**1**) (5 g) was thermally decomposed at 700°C in a muffle furnace. TEM was used to examine the size and shape of the MgO NPs, and powder-XRD (PXRD) was used to confirm the structure.

Antibacterial studies. The antibacterial activity of 6-hpca, the Mg(II) complex, and the MgO NPs against *Escherichia coli* (gram-negative) and *Staphylococcus aureus* (gram-positive) bacteria was investigated in vitro using the disk diffusion method with Mueller Hinton plates. The nutrient agar and broth cultures were prepared as described76,[77] and incubated at 37°C. The SI contains a detailed description of the experimental procedure and conditions. The experiments were carried out in triplicate to ensure reproducibility. As a result, the results were reported as minimum inhibitory concentrations. *Kanamycin* (a common antibiotic) was used as a positive control in the pathogenic studies.

Antioxidant studies. The DPPH free radical-scavenging capacity of **1** and the MgO NPs was systematically evaluated at various concentrations (10, 50, 150, 250, 350, and 500 g/mL) of **1** and the MgO NPs using standard ascorbic acid.[78-81] The experiments were conducted in triplicate, and the DPPH radical concentration was calculated using the equation below:

$$\text{DPPH Scavenging Activity (\%)} = \frac{A_{control} - A_{sample}}{A_{control}} \times 100$$

.

Electrochemical biosensing. The electrochemical responses of the as-prepared **1** and MgO NPs against glucose were measured using a MetrohmAutolab M204 electrochemical workstation. The experiments were conducted at room temperature in a NaOH (0.1 M) supporting electrolyte, with a platinum sheet serving as the counter electrode in a three-electrode system that also included a KCl reference electrode (saturated calomel electrode, SCE) and the Mg complex- or MgO NP-modified GCE as the working electrode. The modified GCE was made by dispersing 10 mL of the compounds onto the surface of the GCE and drying it for 24 h. The Mg complex or MgO NP dispersions were made by sonicating 10 mg of the Mg complex or MgO NPs in deionized water (10 mL) containing 5% Nafion solution (40 mL) for 1 h.[82-87] All the experiments were conducted at room temperature.

Catalytic reduction of 4-nitrophenol (4-NP). The reduction of 4-NP was accomplished by employing MgO NPs as efficient catalysts. At room temperature, 0.1 mg of the catalyst (MgO NPs) was added to an aqueous solution containing 2.7 mL of 4-NP (0.1 M) and 0.3 mL of sodium borohydride ($NaBH_4$, 0.1 M). UV–vis absorption spectroscopy was used to track the progression of the reduction reaction at regular intervals within a scanning range of 250–600 nm. The absorbance peak at 400 nm gradually decreased as the reaction progressed, and the pale-yellow color of 4-NP gradually disappeared every 4 min. When the reaction was finished, the catalyst was extracted using ultracentrifugation. The catalyst was washed with distilled ethanol and vacuum-dried at 60°C for 3 h before reuse. The recovered catalyst from the aforementioned process was tested for stability and reusability by reusing it in the reduction process at various cycles.[88-90]

Conflicts of interest

"There are no conflicts to declare".

Acknowledgments

The authors wish to acknowledge PSGR Krishnammal College for Women, Coimbatore, India for funding the project under the GRG–Trust Project Scheme. Funding from the National Science Foundation (MRI, CHE-1827756) for the purchase of the Venture-Duo diffractometer is acknowledged.

Notes and references

The following is the supplementary data related to this article: Supplementary crystallographic data are available free of charge from The Director, CCDC, 12 Union Road, Cambridge, CB2 1EZ, UK (fax: +44-1223-336033; E-mail:deposit@ccdc.cam.ac.uk or www:http://www.ccdc.cam.ac.uk) upon request, quoting deposition number CCDC 2,082,072.

1. C. Jones, *Nat. Rev. Chem.*, 2017, **1**, 17.
2. A. Stasch and C. Jones, *Dalton Trans,* 2011, **40**, 5659.
3. R. Lalrempuia, C. E. Kefalidis, S. J. Bonyhady, B. Schwarze, L. Maron, A. Stasch and C. Jones, *J. Am. Chem. Soc.,* 2015, **137**, 8944.
4. X. Cao, W. Wang, K. Lu, W. Yao, F. Xue and M. Ma, *J. Org. Chem*, 2020, **49**, 2776.
5. N. S. Poonia and A. V. Bajaj, *Chem. Rev.*, 1979, **79**, 389.
6. R. Custelcean, P. Remy, P. V. Bonnesen, D. E. Jiang and B. A. Moyer, *Angew. Chem. Int. Ed*, 2008, **47**, 1892.
7. Q. Shuai, S. Chen and S. Gao, *Inorg. Chim Acta,* 2007, **360**, 1381.
8. Y. Gao, Z. Dai, J. Zhang, X. Ma, N. Tang and J. Wu, *Inorg. Chem.*, 2014, **53**, 716.
9. P. C. Cheng, F. S. Tseng, C. T. Yeh, T. G. Chang, C. C. Kao, C. H. Lin, W. R. Liu, J. S. Chen and V. Zima, *Cryst. Eng. Commun.*, 2012, **14**, 6812.
10. Y. Fujiwara, S. Horike, K. Kongpatpanich, T. Sugiyama, N. Tobori, H. Nishihara and S. Kitagawa, *Inorg. Chem. Front.*, 2015, **2**, 473.
11. A. A. Yaroshevsky, *GeoChem. Int.,* 2006, **44**, 48.
12. J. Yin, Y. Hu and J. Yoon, *Chem. Soc. Rev.,* 2015, **44**, 4619.
13. K. Revunova and G. I. Nikonov, *Dalton Trans.*, 2005, **44**, 840.
14. G. K. Mor, K. Shankar and M. Paulose, *Nano Lett.*, 2005, **5**, 191.
15. Q. Yang, J. Sha, L. Wang, J. Wang and D. Yang, *Mater. Sci. Eng.*, 2006, **C 26**, 1097.
16. S. S. Lee, S. Y. Lee, J. S. Hyun, C. G. Kim and Y. Kim, *Chem. Vap. Depos.*, 2002, **8**, 257.
17. H. O. Davies, A. C. Jones, T. J. Leedham, M. J. Crosbie, P. J. Wright, N. M. Boag and J. R. Thompson, *Chem. Vap. Depos.*, 2000, **6**, 71.
18. J. H. Boo, S. B. Lee, K. S. Yu, W. Koh and Y. Kim, *Thin Solid Films*, 1999, **341**, 63.
19. M. Vallet-Regí, M. Labeau, E. García, M. V. Cabañas, J. M. González-Calbet and G. Delabouglise, *Phys. C*, 1991, **180**, 57.
20. D. Y. Kim and G. S. Girolami, *Inorg. Chem.*, 2010, **49**, 4942.
21. G. Carta, N. El Habra, L. Crociani, G. Rossetto, P. Zanella, A. Zanella, G. Paolucci, D. Barreca and E. Tondello, *Chem. Vap. Depos.*, 2007, **13**, 185.
22. M. Zhao, X. L. Chen, W. J. Wang, Y. J. Ma, Y. P. Xu and H. Z. Zhao, *Mater. Lett.*, 2006, **60**, 2017.
23. X. S. Fang, C. H. Ye, L. D. Zhang, J. X. Zhang, J. W. Zhao and P. Yan, *Small*, 2005, **1**, 422.
24. A. Subramania, V. G. Kumar, A. R. S. Priya, T. Vasudevan, *Nanotechnology*, 2007, **18**, 225601.
25. Z. Li, C. V. Ciobanu, J. Hu, J.-P. Palomares-Báez, J.-L. Rodríguez-López, and R. Richards, Phys. *Chem. Chem. Phys.,* 2011, **13**, 2582.
26. W. C. Li, A. H. Lu, C. Weidenthaler and F. Schu, *Chem. Mater.*, 2004, **16**, 5676.
27. S. Stankic, M. Muller, O. Diwald, M. Sterrer, E. Knzinger and Bernardi, *Angew. Chem. Int. Ed.,* 2005, **44**, 4917.
28. S. Y. Lee, S. H. Lee, E. J. Nah, S. S. Lee and Y. Kim, *J. Cryst. Growth*, 2002, **236**, 635.
29. J. Miklovič, P. Seg, D. Mikloš, J. Titiš, R. Herchel and M. Melník, *Chem. Pap.,* 2008, **62**, 464.
30. G. Chen, *Z. Naturforsch*, 2008, **63**, 1357.
31. S. K. Verma, K. K. Verma, R. Ram and N. Bhojak, *Chem. Sci. Trans.,* 2018, **7**, 531.
32. S. M. O. Quintal, H. I. S. Nogueira, V. Felix and M. G. B. Drew, *Polyhedron,* 2002, **21**, 2783.
33. P. C. R. Soares-Santos, H. I. S. Nogueira, J. Rocha, V. Felix, M. G. B. Drew, R. A. Sá Ferreira, L. D. Carlos and T. Trindade, *Polyhedron*, 2003, **22**, 3529.
34. M. G. B. Drew, R. A. S Ferreira, L. D. Carlos, T. Trindade, *Inorg. Chem. Commun.* 2003, **6**, 1234.
35. P. D. Balakrishnan, P. Kanchana, N. Arunadevi, N. P. Rath and T. Premkumar, *J. Mol. Struct.,* 2022, **1269**, 133818.
36. S. Long, M. Siegler and T. Li, *ActaCrystallogr. E,* 2006, **62**, o5664.
37. X. L. Zhanga and S. W. Ng, *ActaCrystallogr.* E, 2005, **61**, m1142.
38. X. L. Zhanga and S. W. Ng, *ActaCrystallogr. E,* 2005, **61**, m1140.
39. X. L. Zhanga and S. W. Ng, *ActaCrystallogr. E*, 2005, **61**, m1063.
40. J. Pachiyappan, N. Gnanasundaram and G. L. Rao, *Res. Mater.,* 2020, **7**, 100.
41. C. Shao, H. Guan, Y. Liu and R. Mu, *J. Mater. Sci.*,2006, **41**, 3821.
42. L. Kumari, W. Z. Li, C. H. Vannoy, R. M. Leblanc and D. Z. Wang, *Ceram. Int.,* 2009, **35**, 3355.
43. T. Goryczka, G. Dercz, K. Prusik, L. Pająk and E. Łągiewka, *Solid State Phenom*, 2010, **163**, 177.
44. R. Saravanan, V. K. Gupta, V. Narayanan and A. Stephen, *J. Mol. Liq.,* 2013, **181**, 133.
45. B. Nagappa and G. T. Chandrappa, *Micropor. Mesopor. Mater.,* 2007, **106**, 212.
46. D. H. Ko, S. C. Kang, C. W. Lee and J. S. Im, *J. Ind. Eng. Chem.,* 2022, **112,** 162.
47. A. H. Wani and M. A. Shah, *J. Appl. Pharm. Sci.*, 2012, **2**, 40.
48. S.-W. Bain, Z. Ma, Z.-M. Cui, L.-S. Zhang, F. Niu and W.-G. Song, *J. Phys. Chem. C,* 2008, **112**, 11340.
49. F. Behzad, S. Mortezanaghib, M. A. Jadidikouhbanani, S. Nafisetabatabaei and K. Yoprhee, *J. Ind. Eng. Chem.,* 2021, **94,** 92.
50. M. Tumer, H. Koksal and M. K. Sener, *Transit. Met. Chem.*, 1999, **24**, 414.
51. I. Muhammad, I. Javed, I. Shahid and I. Nazia, *Turk. J. Biol.*, 2007, **31**, 67.
52. N. Sultana, M. S. Arayne, S. B. S. Rizvi, U. Haroon and M. A. Mesaik, *Med. Chem. Res.,* 2013, **22**,1371.

53 G. S. Hikku, K. Jeyasubramanian and S. Vignesh Kumar, *J. Ind. Eng. Chem.,* 2017, **52,** 168.

54 J. Jeevanandam, Y. S. Chan and M. K. Danquah, *Med One*., 2019, **4**, e190011.

55 S. Makhluf, R. Dror, Y. Nitzan, Y. Abramovich, R. Jelinek and A. Gedanken, *Adv. Funct. Mater*., 2005, **15**, 1708-1715.

56 M. Mirhosseini and M. Afzali, *Food Control*, 2016, **68**, 208-215.

57 K. Kavitha, M. Prabhu and Selvam, et al. *Mater. Sci. Eng. C*, 2014, **48**, 252–262.

58 Z.-X. Tang and B.-F. Lv, *Braz. J. Chem. Eng.,* 2014, **31**, 591- 601.

59 G. Huang, T. W. Ng, T. An, G. Li, B. Wang, D. Wu, H. Y. Yip, H. Zhao and P. K. Wong. *Water Res.*, 2017, **118,** 104-13.

60 A. Saravanakumar, M. Ganesh, J. Jayaprakash and H. Tae Jang, *J. Ind. Eng. Chem.*, 2015, **28,**277.

61 N. Ghosh, T. Chakraborty, S. Mallick, S. Mana, D. Singh, B. Ghosh, S. Roy, *Spectrochim. Acta A Mol. Biomol. Spectrosc.*, 2015, **151**, 807–881.

62 S. Roy, S. Mallick, T. Chakraborty, N. Ghosh, A. K. Singh, S. Manna, S. Majumdar, *Food Chem*., 2014, **173**, 1172–1178.

63 G. S. El-Sayyad, F. M. Mosallam, A. I. El-Batal, *Adv. Powder Technol*., 2018, **29**, 2616–2625.

64 S. N. Hosseini, S. Pirsa and J. Farzi, *Polym. Test.,* 2021**, 97**, 107182.

65 A. Umar, M. M. Rahman and Y.-B. Hahn, *Electrochem. Commun*., 2009, **11**, 1353–1357.

66 C. F. Lina, C. H. Kaoa, C. Y. Linb, Y. W. Liua, C. H. Wang, *Results Phys.,* 2020, **16***,* 102976.

67 S. H. Baek, J. Roh, C. Y. Park, M. W. Kim, R, Shi, S. K. Kailas and T. J. Park, *Mater. Sci. Eng. C.*, 2020, **107**, 110273.

68 V. Archana, Y. Xia, R. Fang and G. Gnanakumar, *ACS Sus. Chem. Eng*. 2019, **7**, 6707−6719.

69 B. Wang, S. Li, J. Liu and M. Yu, *Mater. Res. Bull*., 2014, **49**, 521–524.

70 H. Yildirim, E, Guler, M. Yavuz, N. Ozturk, P. K. Yaman, E. Subas, E. Sahin and S. Timur, *Mater. Sci. Eng. C*, 2014, **44,** 1–8.

71 S. A. Hosseini, Z. Shokri and S. Karami, *J. Ind. Eng. Chem.,* 2019, **75,**52.

72 I. Karuppusamy, M. S. Samuel, E. Selvarajan, S. Shanmugam, P. S. M. Kumar, K. Brindhadevi and A. Pugazhendhi, *J. Colloid. Interface. Sci.*, 2021, **584,** 770-778.

73 B. C. Filiz, *Adv. Powder Technol*., 2020, 31, 3845-3859.

74 F. T. Bekena, H. Abdullah, D.-H. Kuo and M. A. Zeleke, J. Ind. Eng. Chem., 2019, 78, 116-124.

75 B. M. Mogudi, P. Ncube, N. Bingwa, N. Mawila, S. Mathebula, R. Meijboom, *Appl. Cat. B: Environmental*., 2017, 218, 240-248.

76 L. H. Abdel-Rahman, A. M. Abu-Dief, R. M. El- Khatib and S. M. Abdel-Fatah, *Bioinorg. Chem.,* 2016, 5, 140.

77 A. W. Bauer, W. M. Kirby and J. C. Scherris, *Am. J. Clin. Pathol.*, 1966, **45**, 493.

78 R. Cruickshank, J. P. Duguid, B. P. Marmion and R. H. A. Swain, *J. Med. Microbiol.,*1995, **11**, 196.

79 F. Ijaz, S. Shahid, S. A. Khan, W. Ahmad and S. Zaman, *Trop. J. Pharm. Res.,* 2017, **16**, 743.

80 S. A. Khan, F. Noreen, S. Kanwal, A. Iqbal and G. Hussain, *Mater. Sci. Eng. C,* 2018*,* **82**, 46.

81 S. A. Khan, S. Shahid, Z. A. Khan and, A. Iqbal, *Int. J. Sci. Res. Publ.*, 2016, **6**, 529.

82 A. Khalid, S. Shahid, S. A. Khan, S. Kanwal, A. Yaqoob, Z. G. Rasool and, K. Rizwan, *Trop. J. Pharm. Res.*, 2018, **17**, 1531.

83 M. Shamsipur, M. Najafi and M. M. Hosseini, *Bioelectrochem*., 2010, **77**, 120.

84 H. Nie, Z. Yao, X. Zhou, Z. Yang and S. Huang, *Biosens. Bioelectron.*, 2011, **30**, 28.

85 L. Kang, D. He, L. Bie and P. Jiang, *Sens. Actuators B*, 2015, **220**, 888

86 Y. Ding, Y. Liu, J. Parisi, L. Zhang and Y. Lei, *Sens. Actuators B*, 2011, **28**, 393.

87 Y. Zhang, Y. Wang, J. Jia and J. Wang, *Sens. Actuators B*, 2012, **171**, 580.

88 P. C. Rath, D. Saikia, M. Mishra and H.-M. Kao, *Appl. Sur. Sci.,* 2018, **427**, 1217.

89 A. A. Kassem, H. N. Abdelhamid, D. M. Fouad and S. A. Ibrahim, *J. Environ. Chem. Eng.,* 2021, **9**, 104401.

90 H. Zhang and X. Hu, *Enzyme Microb. Technol.,* 2018, **113**, 59.